Multimolecular studies of Galactic star-forming regions

Baan, W. A.; Loenen, A. F.; Spaans, M.

Published in:
Monthly Notices of the Royal Astronomical Society

DOI:
10.1093/mnras/stu1897

Monthly Notices
of the
ROYAL ASTRONOMICAL SOCIETY

MNRAS **445,** 3331–3344 (2014) doi:10.1093/mnras/stu1897

Multimolecular studies of Galactic star-forming regions

W. A. Baan,[1,2,3★] A. F. Loenen[1,4] and M. Spaans[4]

[1]*ASTRON, PO Box 2, NL-7990 AA Dwingeloo, the Netherlands*
[2]*Shanghai Astronomical Observatory, 80 Nandan Rd, Xuhui, Shanghai 23000, People's Republic of China*
[3]*Linneaus University, MSI, SE-351 95 Växjö, Sweden*
[4]*Kapteyn Astronomical Institute, PO Box 800, NL-9700 AV Groningen, the Netherlands*

Accepted 2014 September 10. Received 2014 September 10; in original form 2014 March 20

ABSTRACT

Molecular emission-line observations of isolated Galactic star-forming regions are used to model the physical properties of the molecular interstellar medium in these systems. Observed line ratios are compared with the results predicted by models that incorporate gas-phase chemistry and the heating by stellar radiation and non-radiative feedback processes. The line ratios of characteristic tracer molecules may be interpreted using the contributions of two distinct components: a cold (40–50 K) and high-density (10^5–$10^{5.5}$ cm^{-3}) photon-dominated region (PDR) with a nominal UV flux density and a warm (∼300 K) mechanical heating-dominated region (MHDR) with a slightly lower density ($10^{4.5}$–10^5 cm^{-3}). The relative contributions of these structural components are used to model the observed line ratios. Ionized species may be better modelled by adopting an increase of the cosmic ray flux towards the Galactic Centre and the sulphur abundance should depleted by a factor of 200–400 relative to solar values. The line ratios of the Galactic sample are found to be very similar to those of the integrated signature of prominent (ultra)luminous IR Galaxies. The PDRs and MHDRs in the isolated Galactic regions may be modelled with slightly higher mean densities than in extragalactic systems and a higher MHDR temperature resulting from non-radiative mechanical heating. Multimolecular studies are effective in determining the physical and chemical properties of star formation regions by using characteristic line ratios to diagnose their environment. The addition of more molecular species will reduce the existing modelling redundancy.

Key words: surveys – stars: formation – ISM: abundances – ISM: jets and outflows – ISM: molecules – radio lines: ISM.

1 INTRODUCTION

During recent years, much effort has been put into observing and analysing the molecular interstellar medium (ISM) in nearby galaxies (e.g. Solomon, Downes & Radford 1992; Aalto et al. 2002; Gao & Solomon 2004; Graciá-Carpio et al. 2006; Baan et al. 2008; Loenen et al. 2008). Although significant progress has been made in understanding the integrated emissions of these (often unresolved) nuclear regions, their interpretation needs to be benchmarked using comparable Galactic observations.

Many observational studies have been done to interpret the variety of phenomenology of the Galactic ISM. However, most of these studies are not suitable to serve as a general benchmark for interpreting extragalactic observations because they address only a small part of the physical and chemical variety found in the Galaxy. This is usually because the surveys that target a large number of sources or a large area of the sky observe only a limited number of molecular species, with CO and its isotopes being most common (e.g. Solomon et al. 1987; Oka et al. 1998; Simon et al. 2001). On the other hand, multiline surveys are typically limited to a particular small area of the sky (e.g. Jones et al. 2008; Lo et al. 2009).

In this paper, we make a first step towards creating a Galactic data base using a multimolecular survey of isolated star-forming regions. The observed molecules are known to have strong emission lines that are commonly observed in extragalactic studies. The Galactic target sources were taken from a CS(2–1) survey of sources that were identified as ultracompact HII regions (UCHIIRs) based on their infrared properties (Bronfman, Nyman & May 1996). Although the target sources were initially selected to ensure that they form a homogeneous sample of star-forming regions of a similar type, currently available data indicate that the sample is less homogeneous than assumed (see Section 3). Nevertheless, the modelling in this paper will investigate the average molecular characteristics of the sample sources rather than consider the individual sources.

The data will be interpreted using models that incorporate the physics and gas-phase chemistry of the molecular cloud, as well as the radiative transfer for a number of the observed molecular

★ E-mail: willem.baan@shao.ac.cn

species. These models help to determine the physical properties of the clouds and may provide a benchmark for interpreting Galactic star formation regions. These current results may then be compared with those of similar studies of luminous IR galaxies (LIRGs; Baan et al. 2008; Loenen et al. 2008). While some extragalactic systems may have conditions that are too extreme for having Galactic analogues, a correlation may be established between the emission and physical properties of Galactic and extragalactic star-forming regions.

The structure of the paper is as follows. Sections 2 and 3 present the Galactic observations and the source sample; Section 4 describes the physical and chemical models used to interpret the data; Section 5 presents and analyses the properties of the observed lines and the line ratios; Section 6 compares them to extragalactic results; Section 7 presents concluding remarks.

2 OBSERVATIONS AND DATA REDUCTION

The observations of 32 isolated Galactic star formation regions have been carried out using the Onsala 20 m telescope in 2008 April. The mostly low-*J* transitions of nine molecular species observed in the 3 mm window have been tabulated in Table 1. They have been selected based on their observed line strengths in Galactic sources and the potential to detect them in extragalactic sources. Although these transitions may trace some cold gas emission components, they are found to be very prominent in the star formation regions. The strengths of some and potentially all of these transitions make them particularly useful for global modelling of the emission regions.

The observations were done with a 160 MHz bandwidth and a spectral resolution of 100 kHz, which corresponds to velocity width of $\sim$500 km s^{-1} and a spectral resolution of $\sim$0.3 km s^{-1} at 90 GHz. The band was tuned to the rest frequency of the observed line, in order to minimize re-tuning. The observations have been done in position switching mode with 12 × 30 s of integration on both the ON and OFF positions and with chopper wheel calibration preceding every six scans. The total time spent per line per source was about 15 min, including slewing time. Regular calibration of the pointing accuracy (and when atmospheric conditions changed, e.g. weather, sun rise) using five-point scans on SiO maser sources has shown an accuracy of typically $\lesssim$5 arcsec. The size of the beam ranged between 33 (CN) and 44 arcsec (SiO).

Table 1. Characteristics of the observed emission lines.

Molecule	Transition[a]	Frequency (GHz)	Beam (arcsec)	Aperture eff.[b] (Jy K^{-1})
SiO	$J = 2$–1	86.84	43.9	22.1
HNCO	$J = 4$–3	87.93	43.0	22.6
HCN	$J = 1$–0	88.63	42.7	22.8
HCO$^+$	$J = 1$–0	89.19	42.4	23.0
HNC	$J = 1$–0	90.66	41.7	23.4
N_2H^+	$J = 1$–0	93.17	40.6	24.2
CS	$J = 2$–1	97.98	38.6	25.7
C^{18}O	$J = 1$–0	109.78	34.5	29.4
^{13}CO	$J = 1$–0	110.20	34.3	29.5
CN	$N_J = 1_{3/2}$–$0_{1/2}$	113.49	33.3	30.5

[a]For transitions that are split, all sub-levels were combined.
[b]Obtained by interpolating between documented values.

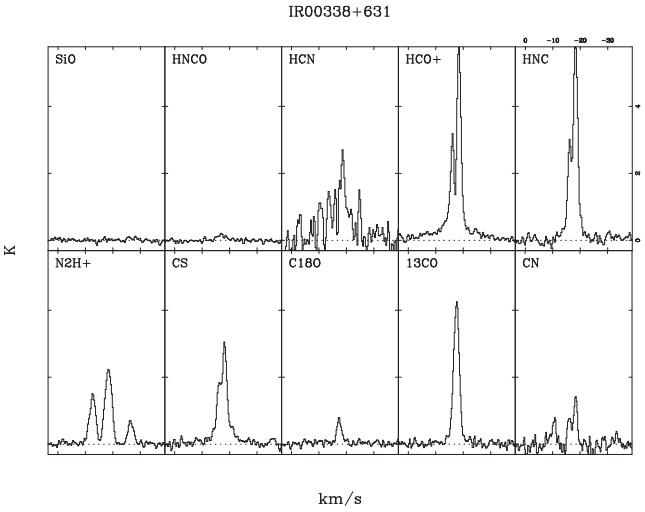

Figure 1. Spectral data obtained from the source IRAS 00338+631 and representative of the rest of the sample. The spectra are displayed as main beam temperature T_{MB} in K. The velocity and intensity scales are depicted in the upper-right frame and they apply for all frames.

The data have been reduced using the XS package.[1] After averaging all scans of one observation, baselines were subtracted by fitting first-order polynomials. Higher order baselines were used in some cases when the baseline showed significant structure. The resulting spectra are presented in Appendix B available online as Supporting Information. An example of the spectral data for one of the sources is presented in Fig. 1. The integrated line strengths of the emissions have been determined by fitting Gaussian line profiles to the main spectral components and the results are presented in Table A1 in energy units of Jy km s^{-1}. For observed lines exhibiting sub-level transitions, all sub-level transitions were combined to obtain the total integrated line strength. Because this study only considers the ratios of the integrated values, the (mostly small) variation of the line width for the lines of each source is not taken into account and the details of individual line width and line strength are not presented. Indeed, any comparison of the integrated properties of Galactic sources with those of extragalactic sources strongly depends on the line width but the line ratios for a particular source do not.

Some of the CS observations have been taken during inclement weather conditions, resulting in lower signal to noise ratios and several non-detections. The shock tracer HNCO has weak detections for five sources, and the shock tracer SiO has been observed in 10 sources with only 2 weak detections using (very) limited observing time.

3 THE SOURCE SAMPLE

The Galactic target sources from the CS(2–1) survey have been initially identified as a homogeneous sample of star formation regions classified as UCHIIRs, based on their IR properties (Bronfman et al. 1996). Currently available data indicate that the sample is less homogeneous than assumed because the classification solely on the basis of *IRAS* colours is not fully reliable (e.g. Ramesh & Sridharan 1997; Bourke, Hyland & Robinson 2005). In particular, high-mass protostellar objects that did not yet develop a significant

[1] http://www.chalmers.se/rss/oso-en/observations/data-reduction-software

UCHIIR can show UCHIIR-like colours (Sridharan et al. 2002). As a result, the current sample of sources has been indicatively classified using SIMBAD[2] as UCHIIRs(11), young stellar objects (YSOs; 4), Herbig–Haro objects (1), dense cores (2), or simply IR sources (14). Many of the sample sources exhibit evidence of molecular outflows (e.g. Beuther et al. 2002; López-Sepulcre, Cesaroni & Walmsley 2010), while the radio continuum emission anticipated for an UCHIIR is not always detected or may be displaced from the dust emission (e.g. Sridharan et al. 2002).

The sources in this heterogenous sample are considered to be at relatively early stages of development having a clear UV-dominated component driven by the star formation, even if the associated radio UCHIIR may not (yet) be prominent. In addition to a common photon-dominated region (PDR) component, some or all sources may contain a structural component that is dominated by outflow-related mechanical heating. The relative prominence of the emissions of both components will vary from source to source. Considering that the classification for all individual sources and the identification of structural components are still incomplete, the integrated properties of the sample sources will be used for modelling their measured line ratios in order to investigate the average molecular characteristics, and to determine trends in the modelling results. At a later stage, this blind study will be followed by detailed modelling of individual sources to further explore these trends.

The evaluation of the presence of any mechanically heated region would have been helped by detections of the two shock tracers HNCO and SiO. However, although other authors have made SiO(2–1) detections for several of the sample sources (Codella, Bachiller & Reipurth 1999; Qiu et al. 2007; Reid & Matthews 2008; López-Sepulcre et al. 2011), the number of detections for HCNO and SiO remains small and the results could not be incorporated further in this paper. Similarly, detections of atomic ions could not be incorporated because of unavailability of the data.

4 MODELLING APPROACH

The ISM has many different phases which are determined by the equilibrium between various cooling and heating processes (e.g. Field, Goldsmith & Habing 1969; Wolfire et al. 1995; Spaans 1996). The ISM is continuously heated by radiation (e.g. stellar UV radiation, X-rays, cosmic rays), by feedback from star formation (e.g. superbubbles, winds, supernovae; see Norman & Ferrara 1996), and by other mechanical processes (e.g. cloud–cloud collisions, shearing motions). Despite this heating on a large scale, 'condensations' form on smaller scales (e.g. Wada & Norman 2007), leading to cold, dense, molecular cores, which become the sites of star formation. During their protostellar evolutionary phase, the stars will also inject energy into the surrounding ISM. Once a star is formed, the stellar UV radiation creates a PDR (Hollenbach & Tielens 1999) with a decreasing radial temperature gradient because of the attenuation of the UV radiation field by gas and dust.

The sources in our sample are expected to contain such a (small-scale) PDR embedded within the dense molecular clouds that are hot nearby the central star and colder further away (a 'classical' PDR). Some or all these PDRs may be accompanied by a mechanical heating-dominated region (MHDR) that contains lower density and warm molecular gas that is heated by mechanical feedback from the outflows of protostellar objects. The presence of both components is required for these sources to explain the range in the observed line ratios and also their variation with distance (see Section 5.1). In the current modelling approach, two independent models are calculated: the UV-radiation-driven PDR and the feedback-heated MHDR using density, column density, mechanical heating, and UV flux as variables. Each of the models independently considers the physics and chemistry of the region, evaluates the abundance and the radiative transfer of each of the molecules within the model component. The emission characteristics of a source are then found by adding together the individual line contributions from both the PDR and the MHDR model components using a certain mixing ratio and determining the line ratios from the combined line contributions.

The modelling procedure produces the combined line strengths of the source and the ratio of distinct PDR and MHDR components with different environment parameters and different relative strength. At one extreme, the source will be a pure PDR without any MHDR component and at the other extreme the source has a 90 per cent MHDR component with a 10 per cent PDR component. Detailed modelling of individual sources and their energetics requires that the observed line strengths, the infrared details, the observed size of the source, and the prominence of the UCHIIRbe also taken into account. The current PDR+MHDR models do not (yet) rule out some alternative scenarios (not to be considered in this paper) for explaining the line ratio behaviour, such as employing cosmic ray (CR) and X-ray heating rather than mechanical heating, gas–grain chemistry, or shock physics, which will be less important for low-J transitions. In addition, the inherent redundancy of the modelling approach results from the limited molecular input data. The inclusion of additional molecular and atomic transitions would allow the recognition of more physical processes and increase the accuracy of the modelling.

4.1 PDR models

The PDR models are created using the models as described in Loenen et al. (2008), which are based on the work by Meijerink & Spaans (2005) and Meijerink, Spaans & Israel (2007). The total column density along a line of sight in the cloud was chosen to be of the order of 10^{22}–10^{23} cm^{-2}, which corresponds to a visual extinction from 6–55. At such high column densities, the observed lines become optically thick and predominantly trace the outer regions of the PDR, where the impinging stellar radiation is severely attenuated. This implies that, as discussed in Loenen et al. (2008), variation of the intensity of the UV radiation field (6–13.6 eV; Habing 1968; Draine 1978) of the PDR does not alter the results significantly. Adopting the UV flux density of 160 erg s^{-1} cm^{-2} used in these models, the density of the PDR component is constrained by using the HCO$^+$/HCN and HCO$^+$/HNC line (Section 5.2) ratios and is found to lie within the range of 10^5 and $10^{5.5}$ cm^{-3} for all sources. The CR flux used for the PDR models equals that of the solar neighbourhood ($\zeta = 5 \times 10^{-17}$ s^{-1}). While the CR heating can become significant at the highest column densities in cold environments, the CR flux also affects the ionization balance and influences the abundance of the ionized molecular species in the data. The current PDR models do not incorporate X-ray heating term, which would further change the chemistry.

The single-component PDR models assume that the dominant emissions for the various molecules originate in the same volume of space having an environment with mean values. Possible emission contributions from regions with diverging environmental conditions are not considered, such as HCN and HNC emission from regions with low ionization and high extinction.

[2] http://simbad.u-strasbg.fr/simbad/

4.2 MHDR models

In order to model the MHDRs, a variation on the Loenen et al. (2008) code was made, in which the gas temperature is not determined by the UV radiation field in the PDRs. Instead, the gas temperature is increased due to the mechanical heating. At high densities ($>10^{4.5}$ cm^{-3}), the gas and dust temperatures are coupled, resulting in heating of the dust by the warm gas. This leads to a chemistry that is significantly different than that found in PDRs, in particular in the considerable decrease of the HNC/HCN and HCO$^+$/HCN ratios as a result of mechanical heating in regions with densities of $n > 10^5$ cm^{-3}. At temperatures higher than 100K, HNC is efficiently converted into HCN (HNC+H→HCN+H; Schilke et al. 1992; Talbi, Ellinger & Herbst 1996) resulting in lower line ratios. Since this effect of dust heating by gas is not included in the Loenen et al. (2008) models, a further approximation was made by fixing the gas and dust temperature in the MHDRs. The absence of detections of SiO and HNCO shock tracer emissions for a significant fraction of the sample does not facilitate direct diagnostics of the mechanical heating processes.

The best fits for these MHDRs have been obtained using a slightly lower density (between $10^{4.5}$ and 10^5 cm^{-3}), and a gas/dust temperature of at least 250 K. A degeneracy exists between the temperature of the gas and dust in the MHDR and its relative contribution to the line ratios: a small contribution by a warmer MHDR produces the same line ratios as a larger contribution of a cooler MHDR. For the current models, a temperature of 300 K has been adopted, which is the lowest temperature (and requires the lowest input energy) that allows separating the contributions of the PDR and the MHDR to the line ratios. Clumped dense molecular gas with kinetic temperatures ranging from ∼150 up to ∼240 K has actually been observed (e.g. in NGC 253; Ott et al. 2005). In the absence of spatial information, these are average (global) properties, because the heating process is likely to be inhomogeneous and to lead to a part of the MHDR being hotter and a part being cooler than 300 K.

The MHDR models in this study and in the shock-heated PDR models for extragalactic environments (Loenen et al. 2008) adopt a fixed kinetic temperature resulting from the mechanical heating. Rather than adopting a temperature, Kazandjian et al. (2012) has adopted a more self-consistent approach by adding a separate mechanical heating term to the environmental modelling, and predicting mechanically induced temperatures in the 100–300 K range. The results for our simplified models are consistent with this temperature range. While the low-J transitions of these molecules may (predominantly) trace cooler gas, the emission lines at higher temperatures are equally strong and they do confirm the predicted decrease of the HNC/HCN and HCO$^+$/HCN abundance ratios as a result of mechanical heating. Alternative schemes based on CR and collisional processes to account for the heating of the molecular medium may be found in the literature (Ferland et al. 2009; Bayet et al. 2011).

The combined PDR and MHDR models can explain the observed HNC/HCN line ratios very well, but the observed HCO$^+$/HCN line ratios for sources closest to the Galactic Centre (GC) are found to be slightly higher than the model predictions when using the CR ionization flux of the solar neighbourhood. The chemistry of HCO$^+$, and also of N_2H^+, strongly depends on the ionization balance, and sources close to the GC could be exposed to a higher CR flux. An estimated value for the CR ionization rate at the GC may be even two orders of magnitude higher than that of the solar neighbourhood at $\zeta = (2\text{–}7) \times 10^{-15}$ s^{-1} (Oka et al. 2005). However, within large uncertainties and scatter, there is evidence that the CR ionization rate decreases with increasing column density as the low-energy CR are attenuated (e.g. Padovani & Galli 2013). As a result, the CR ionization rate could be about 10 times higher in diffuse gas than in denser clouds.

An increase in the CR ionization rate will lead to increased dissociative recombination of HCO$^+$ with electrons but also direct ionization may lead to increase of ions. At the density range found for our sources, the HCO$^+$/HCN and HCO$^+$/HNC line ratios will increase, while at lower densities ($n \approx 10^4$ cm^{-3}) the ratios will decrease (Meijerink, Spaans & Israel 2006; Loenen et al. 2008). However, the high column densities of the PDR and MHDR may again reduce these effects. Variations of the CR flux has been incorporated in the models in a simplified manner. Instead of generating (computationally intensive) grid of models for sources at different $R_{\rm gal}$ and CR rates, the CR ionization rate is assumed to be solar for the PDR and at the level of the GC for the MHDR. For (more distant) sources, which we expect to have a higher MHDR contribution (see Section 5.1), this approximation may describe the CR rate dependence on $R_{\rm gal}$. The contribution of the MHDR to the line ratios will thus be affected by both mechanical and CR heating terms. The introduction of an enhanced CR flux density for the MHDR-dominated regions increases the predicted values for the HCO$^+$/HCN and HCO$^+$/HNC ratios by a factor of 2. For comparison, the mechanical heating term in the MHDR contribution reduces the HNC/HCN line ratio by a factor of up to 3.

4.3 Energetics of the MHDRs

In order to validate the possibility that protostellar outflows can be responsible for the heating of the MHDR, we consider the energetics of such a process. The heating rate required to keep the gas at ∼300 K may be determined using the results of Loenen et al. (2008) as $\Gamma_{\rm mech} = 3 \times 10^{-19}$ and 4×10^{-18} erg s^{-1} cm^{-3}, respectively, for $n = 10^{4.5}$ and 10^5 cm^{-3}. Typically, a low-mass outflow can transfer maximally about 10^3 L$_\odot$ to the surrounding molecular medium but the mean value is about 50 L$_\odot$ (Wu et al. 2004), which could maintain a spherical volume with diameter 0.55 pc ($n = 10^{4.5}$ cm^{-3}) or 0.23 pc ($n = 10^5$ cm^{-3}) at the required temperature. An ensemble of outflows may be required to heat a larger volume.

The broad-band *IRAS* colours of our sources (taken from the *IRAS* Point Source Catalog; Beichman et al. 1988) show evidence for dust at such high temperatures. Nearby sources that may be dominated by a PDR component have colours indicating colder dust as compared to more distant sources that may have a larger MHDR contribution, which show relatively enhanced 12 μm emission. More extended MHDRs would significantly contribute to the fluxes measured with the 30 arcsec beam of the *IRAS* 12 μm survey. Ultraluminous IR galaxies (ULIRGs) show a similar enhancement, which can only be attributed to a dust component with temperatures around 400 K (Loenen, Baan & Spaans 2006).

Besides the dust contained in the hottest layers of the PDR, the dust contained in the MHDR could also contribute to the measured *IRAS* 100 μm emission. The gas mass contained in a representative 0.55 pc heated sphere ($n = 10^{4.5}$ cm^{-3}) would be 2.2×10^2 M$_\odot$. Assuming a gas-to-dust ratio of about 100 and with 100 per cent of the dust emitting, the standard dust parameters (e.g. Devereux & Young 1990) predict a 100 μm flux of $2.4 \times 10^6/D^2$ Jy (distance D in kpc). For comparison, the well-known source IRAS 19446+2505 from our sample at an estimated distance of 7.6 kpc would have a predicted flux captured in a 2 arcmin beam of 1.2×10^4 Jy, which is quite consistent with the observed *IRAS* flux of 1.3×10^4 Jy.

In this manner, the far-infrared (FIR) emission properties will provide additional information about the structure of the emission regions.

5 LINE DIAGNOSTICS

5.1 Correlations of line ratios with distance

The line ratios of the high-density tracers suggest various degrees of variation with distance as shown in Fig. 2, which indicate global variation of the environment within the Galaxy. Although there are a few non-conforming data points, all line ratios plotted in Fig. 2 show evidence of a decrease with increasing distance D and all except the N_2H^+/HCN ratio also show an associated increase with the galactocentric distance $R_{\rm Gal}$. Beyond 2–3 kpc, the line ratios may decrease with distance by a factor of as much as 5, except the HCO^+/HCN ratio shows a relative increase at larger distances ($D > 10$ kpc). In addition to their dependence on distance, some of the molecular data show a bifurcation of the data points, with a high and a low value for the ratio. The CS/HCN, CN/HCN, and N_2H^+/HCN ratios show this behaviour with D, while HNC/HCN and possibly N_2H^+/HCN and CS/HCN show this with $R_{\rm Gal}$. This systematic spread suggests further diversification of the local environment, which is not addressed by the modelling of this paper.

A simple variable that could account for the variation of the line ratios with distance is the relative fraction of the beam covered by the PDR and MHDR components. Assuming a PDR component of 0.4 pc, the sampling area of the observing beam becomes larger than the PDR at a distance of 2–3 kpc (i.e. the distance at which the trends set in), and would sample more of any surrounding MHDR component. PDR components for sources at a distance of 10 kpc, and close to the GC, will then cover only 4 per cent of the observing beam. For illustration of such a geometrical model, Figs 2(a)–(c) depict the expected HCO^+/HCN, HNC/HCN, and CS/HCN ratios using the same physical parameters as used in Sections 5.2 and 5.3. Hereby, it has been assumed that the MHDR surrounding the PDR has a size of at least 2 pc (i.e. the beamsize at 10 kpc), and that the CR flux is higher in the MHDR than in the PDR as explained in Section 4.2. While geometrical models may predict the general trends, they do not satisfactorily cover the data points.

On the other hand, our PDR–MHDR models employing the relative contribution of the components also account for the observed line ratios, but they do not carry general implications about the required sizes and geometry of the components. However, the variation in the line ratios does imply that the prevailing environment of sources closer to the GC may be different from the local environment and, particularly, that the conditions of the MHDR components are different from those of the PDRs.

No clear trends were found when comparing the ^{13}CO and C^{18}O data to the high-density tracers (see Appendix A). The ^{13}CO/C^{18}O ratio also remains relatively constant with distance in the current sample (Fig. A1). Since both CO lines trace a large-scale component of the ISM, this ratio does not necessarily relate to the star formation activity and will not be considered further.

5.2 HCN, HNC, and HCO^+ characteristics

The observed HCO^+(1–0)/HCN(1–0), HNC(1–0)/HCN(1–0), and HCN(1–0)/HCO^+(1–0) line ratios for this Galactic sample are plotted against each other in Fig. 3. While the chemistry of HCN and HNC are related and depend strongly on the temperature, the chemistry of HCO^+ is distinctly different and is affected, among other effects, by the ionization state of the environment. Therefore, these diagrams represent the behaviour of HCO^+(1–0) using HCN(1–0) and HNC(1–0) for comparison. The line ratios displayed represent the integrated equilibrium abundance of each of the molecules subjected to the radiation transfer for a representative column density in the source.

Initial analysis of this Galactic data can be done in a similar manner as was done for the extragalactic observations in Loenen et al. (2008). A group of pure PDR models would then occupy the ratio parameter space close to the dotted lines towards the right-hand side of the distribution in the figures. For log(HNC/HCN), these would cover the range from 0.0 to 0.3. The remaining parameter space towards the left in the figures would be occupied by models that combine PDR and MHDR components into the model line ratios, which for log(HNC/HCN) covers the range from 0.3 to 0.8.

Instead of displaying the modelling results for separate PDRs and MHDRs, the results are presented here as a mixing envelope, where mixing is achieved by adding the line contributions from a separate PDR and MHDR models using a certain ratio in order to determine the line ratios. The upper boundary of the envelope in Fig. 3 is formed by the combination of a PDR model with $n = 10^{5.5}$ cm^{-3} and an MHDR model with $n = 10^5$ cm^{-3} (red traces), while the lower boundary is formed by the combination of a PDR model with $n = 10^5$ cm^{-3} and an MHDR model with $n = 10^{4.5}$ (blue traces). All data points lie within the boundaries created by these two model mixing lines for a range of mixing ratios.

In the diagrams, the emission-line ratios predicted for a limited range of the PDR column density (10^{22-23} cm^{-2}) trace the two boundaries, with the highest column density indicated by the dot. The sequential tracks along the boundaries in between the pure PDR extreme at the right-hand side of the diagrams (close to the dotted lines) and pure (or dominant) MHDR extreme (towards the left of the distribution) represent increasing mixing ratios (0, 50, 90, 95 per cent) of the MHDR and PDR components. Considering that each of these tracks extends to much lower column densities, about half the sources would require a significant (>50 per cent) contribution from the MHDR component.

The model variables used in the diagrams (Fig. 3) are primarily the density of the PDR and the MHDR components, the column density for both components, and the mixing ratio. Under the assumption that the molecules occupy the same volume, the density accounts for the variation across the distribution and data points between the boundaries require intermediate model densities. The actual size of the emission regions does not affect the ratios and only the model column density and the mixing ratio accounts for the variation along the distribution.

The HCO^+/HCN ratio (frame a) depends mostly on the gas density such that there is little difference between the MHDR and PDR contributions. As a result the sample appears very homogeneous in terms of density, with only half an order of magnitude spread. Given the error on the measurements, this spread is most likely an intrinsic variation in the sources. Baan et al. (2008) suggested that the average molecular gas density of star-forming regions decreases during their evolution. If this also applies to the sources of the current Galactic sample, then the small range in density translates into a small range of age, which indicates that these sources are indeed at similar and early stages of evolution.

The HNC/HCN ratio (frame c) is insensitive to the gas density but is a strong function of the gas temperature, which differentiates the contributions of a PDR and an MHDR. PDR models with a larger range of column densities can account for HNC(1–0)/HCN(1–0) ratios larger than typically 0.5, but they cannot account for any lower

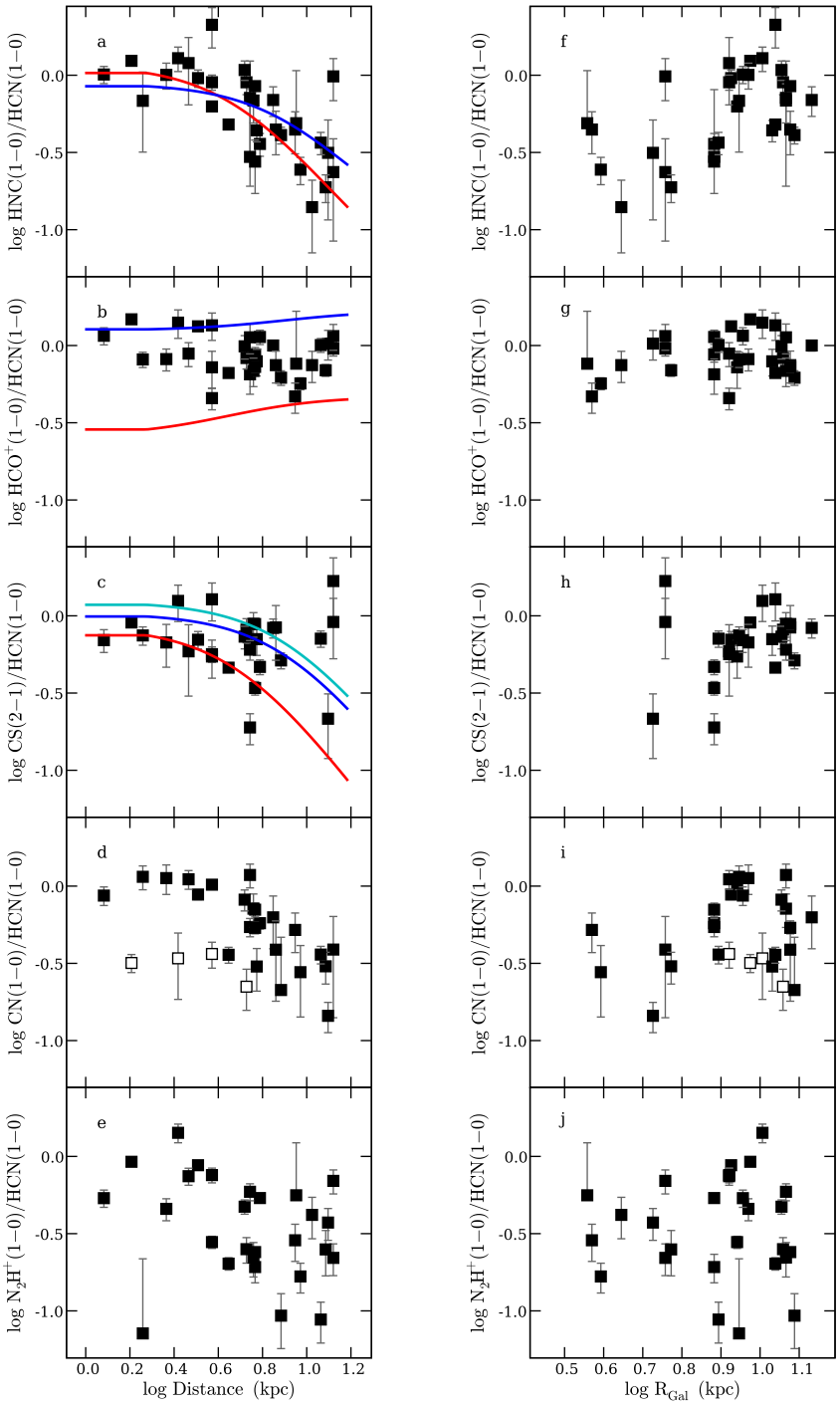

Figure 2. Integrated line ratios for the sample sources plotted as a function of distance (left) or the distance to the GC (Galactic radius, right). The two coloured lines in panels (a) and (b) illustrate simple geometrical PDR–MHDR model predictions for the ratios of HCN, HNC, and HCO^+, assuming a fixed size for the PDR and MHDR components (see Section 5.1 and Fig. 3). The three coloured lines in panel (c) correspond to the geometrical PDR–MHDR model predictions for the CS/HCN ratio using the three scenarios for sulphur depletion presented in Section 5.3. The open CN/HCN data points in panels (d) and (i) represent sources that do not follow the general decrease with distance as also seen in Fig. 5. The line ratios are determined using energy units of Jy km s^{-1}.

values. On the other hand, an additional mechanical heating contribution to the PDR itself can indeed account for some of the lower values of this ratio (Loenen et al. 2008). However, the lowest values of the observed HNC(1–0)/HCN(1–0) ratio can only be accounted for with a separate high (dust) temperature MHDR component, because HNC is efficiently converted into HCN at temperatures higher than 100 K (Schilke et al. 1992; Loenen et al. 2008).

On the other hand, HNC/HCN ratios larger than unity may result from the pumping of the rotational levels of HNC through the mid-infrared continuum (Aalto et al. 2007; Weiß et al. 2007) or from

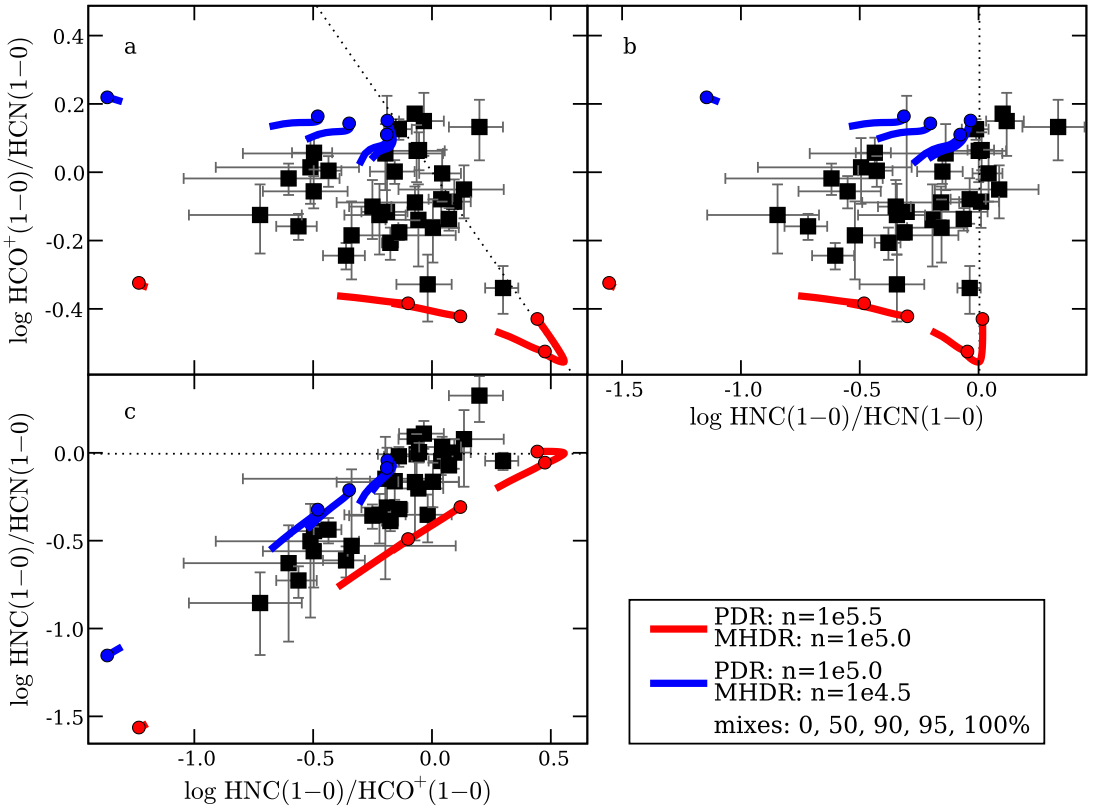

Figure 3. Diagnostic diagrams using integrated line ratios of HCN, HNC, and HCO^+ versus each other. (a) Integrated HCO^+/HCN versus HNC/HCO^+ ratios, (b) integrated HCO^+/HCN versus HNC/HCN ratios, and (c) integrated HNC/HCN versus HNC/HCO^+ ratios. Coloured lines show two PDR plus MHDR models and the mixes between them. The model results are shown as function of column density, with the highest column density indicated by the dot. Pure PDR model results are closest to the dotted black line and those furthest away are dominated by MHDR components. The legend denotes the density n in cm^{-3} for the models.

X-rays influencing the abundances of HNC (Loenen et al. 2008). Pumping of HNC requires brightness temperatures of $T_B \geq 50$ K at 21.5 μm, which are common in ultraluminous galaxies but may not play a role in these Galactic environments. Only four of the Galactic sources show HNC/HCN line ratios slightly above unity. Given that many processes in star formation regions produce X-rays (e.g. protostars, pre-main-sequence winds, outflow shocks, stellar remnants; see Broos et al. 2007, for X-ray observations of the M 17 star-forming region), and the fact that X-rays have a very small absorption cross-section, it is likely that a modest X-ray background may account for the slightly raised HNC/HCN line ratios. Since the effect of X-rays cannot be identified in most sources because of their intrinsically low HNC/HCN ratios and because the effect is modest in those sources where it can be identified, this aspect has not been included in the modelling. Also the effect of a higher CR flux on these ratios needs to be investigated further.

The data points in Fig. 3 show smaller spread in HCO^+/HCN ratios and a larger spread in HNC/HCN line ratios than the extragalactic sources, which confirms the enhanced temperatures due to additional non-radiative heating processes (Loenen et al. 2008). About half of the data points show HNC/HCN and HNC/HCO^+ ratios that are significantly lower than would be obtained for the shock-heated extragalactic models. Only direct shock heating in the MHDR components provides the required increase (factor about 2) for modelling the HCO^+/HCN ratio and a decrease (factor up to 3) of the HNC/HCN ratio. On the other hand, the improvement resulting from a change in the CR flux density in the MHDR models is only marginal and of the same order as the intrinsic spread in the data, which may alternatively result from variation of the density. In addition, the few data points with the lowest values of the HCO^+/HCN line ratio in Figs 2(b) and (g) have a low R_{Gal} and are located near the lower edge of the mixing boundaries (in Fig. 3a) where they require a relatively small MHDR component. Direct heating in the MHDR components should be confirmed by the presence of shock tracers SiO and HNCO in this sample and the presence of protostellar outflows in these targets (see Bachiller & Perez Gutierrez 1997).

5.3 CS characteristics

The CS molecule has a distinctly different chemistry from the other molecules and has a different dependence on the environmental parameters. The observed line ratios of CS(2–1) using HCN (1–0) and HNC(1–0) as references in Fig. 4 display some systematic trends similar to those of the HCO^+ diagrams (compare with Fig. 3). However, the spread in the data points is larger than for HCO^+. The sample has missing data points because some sources at large distances (and low R_{Gal}) could not be observed due to inclement weather (see also Figs 2c and h). These data points would be expected to fill the gap between the main body and the two outlier points with low CS/HCN ratios. The clearly deviant line ratios of IRAS 18151−1208 shown in Figs 4(b) and (c) may result from less than optimal weather conditions.

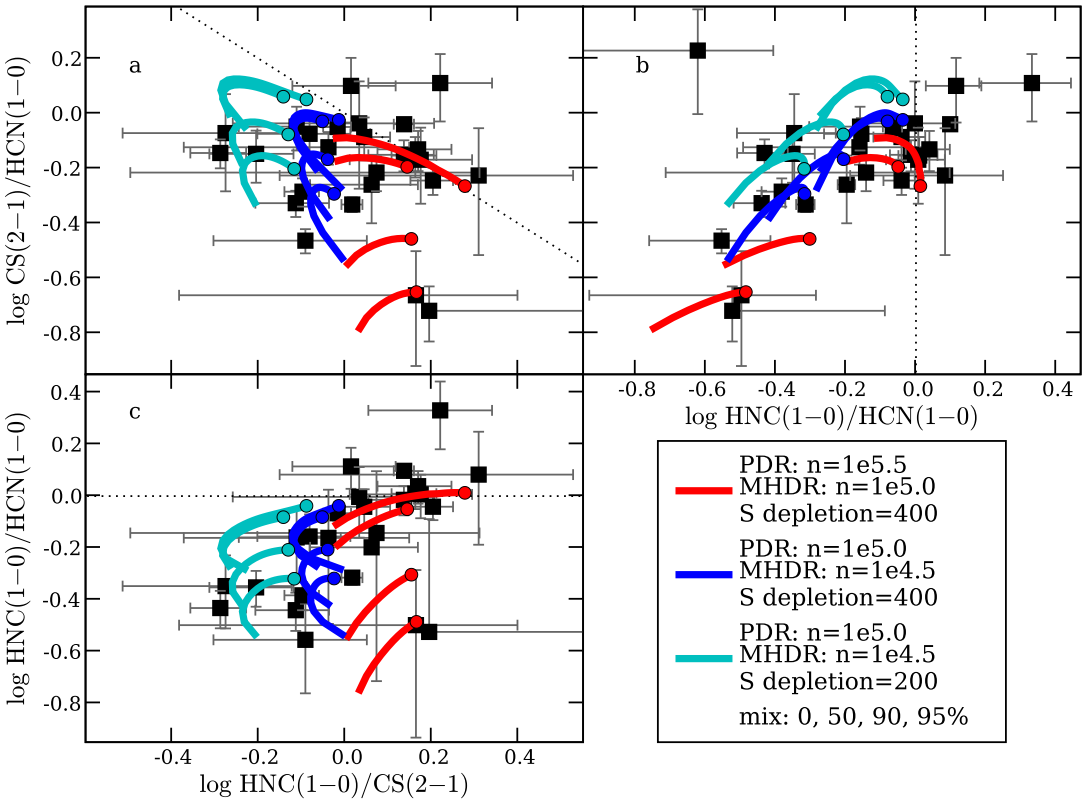

Figure 4. Diagnostic diagrams using integrated line ratios of HCN, HNC, and CS versus each other. (a) Integrated CS/HCN versus HNC/CS ratios, (b) integrated CS/HCN versus HNC/HCN ratios, and (c) integrated HNC/HCN versus HNC/CS ratios. Overplotted are three sets of model results, for different combinations of density and S-depletion. The model results are shown as function of column density, with the highest column density indicated by the dot. Model results closest to the dotted black line are pure PDRs, and those furthest away are dominated by MHDR components. The legend denotes the density n in cm^{-3} used in the models.

In order to interpret the observed CS line ratios, the earlier models (Loenen et al. 2008) have been extended to include the radiative transfer for the CS molecule and the relative abundance of sulphur as a variable. In dense molecular clouds, the sulphur abundance in the gas phase can be lower than in the solar neighbourhood by up to a factor of 1000 (e.g. Gondhalekar 1985; Tieftrunk et al. 1994; van der Wiel et al. 2009), possibly due to S^+ depletion on charged grains (Ruffle et al. 1999). However, there is evidence that the depletion is not as extreme in PDR sources. The nearby Horsehead PDR (driven by a single O9.5 star) has a very low depletion (factor of 4; Goicoechea et al. 2006).

The combined PDR and MHDR models described in this paper assume sulphur depletion of a factor between 200 and 400 w.r.t. solar abundances in order to produce the observed line ratios of CS(2–1) with the other tracer molecules (Fig. 4). If no S-depletion is used, the predicted values would have been about a factor of 10 larger than the observed CS(2–1) line strengths. The model results are again displayed as a function of the column density, with the highest value indicated by the dot. As can be seen, there is a degeneracy between the gas density and the S-depletion. However, since the density was already determined using the HCO^+/HCN and HCO^+/HNC line ratios, an accurate estimate of the S-depletion could be made using only a single S-bearing molecule.

5.4 CN characteristics

The CN chemistry is closely related to that of HCN and HNC and its abundance is strongly affected by the UV radiative flux. This makes CN more of a surface tracer, a comparison between CN and other molecules serves as an added tool to differentiate the environment of the sources. The observational data show a roughly linear correlation between CN/HCN and HNC/HCN with the exception of the four sources marked with white squares (Fig. 5a). This data distribution is similar to those found for the HCO^+(1–0)/HCN(1–0) and CS(2–1)/HCN(1–0) ratios (compare with Figs 3b and 4b). However, a larger spread in the data points and a larger range for the CS(2–1)/HCN(1–0) ratio will provide increased discrimination. The data appear consistent with an increasing relative contribution of an MHDR component at larger distance. The observed CN/HCN line ratio shows a general decrease with distance in Fig. 5(a), similar to the HNC/HCN ratio. However, four distinct sources have ratios that are a factor of 3 lower than the other sources. These four sources at small distances are also distinct in Fig. 5. Their deviant CN/HCN line ratios could result from geometrical properties of the sources, but alternatively, they may mark a lower CN/HCN boundary resulting from variations in the UV field strength.

The model codes used in this paper include the chemical network of CN but do not yet include its radiative transfer, although the collisional rates are already available (Faure & Lique 2012). However, the abundance diagrams of CN and HCN for the PDR and MHDR models already provide a first-order interpretation of the observed CN line ratios (Fig. 6). They show that, for most column densities, the CN abundance peaks at lower column density ($\log(N) \sim 21.4$) than HCN, which peaks deeper into the cloud ($\log(N) \gtrsim 21.8$). This result confirms that CN is more a surface tracer than a volume tracer

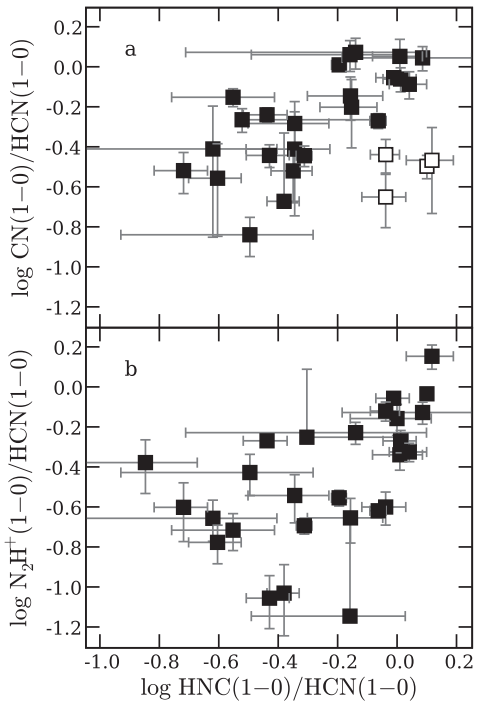

Figure 5. Diagnostic diagrams using integrated line ratios of CN, N_2H^+, HCN, and HNC, similar to Figs 3(b) and 4(b). (a) Integrated CN/HCN versus HNC/HCN ratios, and (b) integrated N_2H^+/HCN versus HNC/HCN ratios.

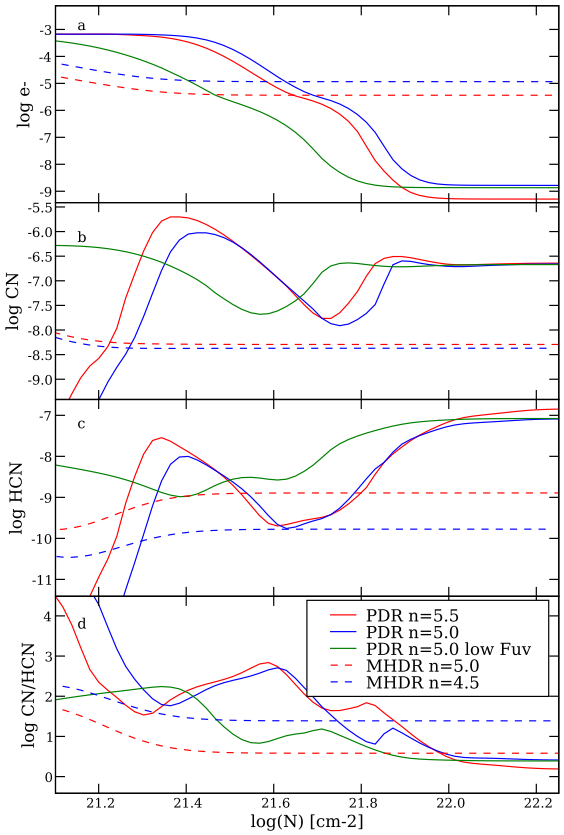

Figure 6. Fractional abundances and abundance ratios for PDR and MHDR models as a function of column density: (a) the electron abundance to be discussed in relation to N_2H^+, (b) the CN abundance, (c) the HCN abundance, and (d) the CN/HCN abundance ratio. All PDR models have $F_{UV} = 160$ erg s^{-1} cm^{-2} except for the 'low F_{UV}' model with $F_{UV} = 1.6$ erg s^{-1} cm^{-2}; n denotes the log of the density in cm^{-3}.

in such dense environments (e.g. Sternberg & Dalgarno 1995). As a result, the CN line strength is more sensitive to the geometry of the source than a volume tracer like HCN, which may explain the complex behaviour seen in the diagram (Fig. 5a).

An important formation route of CN is the photodissociation of HCN and HNC (Sternberg & Dalgarno 1995; Woodall et al. 2007) and the connection between the CN/HCN ratio and the presence of UV photons has indeed been established observationally in both Galactic and extragalactic environments (Fuente, Martin-Pintado & Gaume 1995; Fuente et al. 2005). Fig. 6 shows that a PDR with a lower UV flux (green lines, $F_{UV} = 1.6$ erg s^{-1} cm^{-2}) also has a lower CN/HCN abundance ratio throughout most of the cloud.

Fig. 6 also shows that for most column densities, the CN/HCN abundance ratios are lower in the MHDRs than in the PDRs. However, since the CN is a surface tracer for both the MHDR and PDR, radiative transfer modelling needs to confirm that lower abundance ratios translate into lower emission-line ratios and that the inclusion of MHDR contributions has a lowering effect on the CN/HCN ratio. Nevertheless, the CN/HCN line ratio will serve as a valuable addition to the existing HCN, HNC, and HCO^+ diagnostics, which are not sensitive to the UV radiation field.

5.5 N_2H^+ characteristics

As a second ion in our survey, N_2H^+ has a different chemistry showing a strong dependence on the ionization level of the source environment and providing another independent addition to the diagnostic modelling. The N_2H^+/HCN data displays a similar distribution as the equivalent diagrams for HCO^+(1–0), CS(1–0), and CN(1–0) except that the spread in the data points is significantly larger and the range for the N_2H^+/HCN ratio is larger than for the other molecules (Fig. 5). This is consistent with the general decrease of the N_2H^+/HCN line ratio with distance and the (apparent) division in high and low data points found in Fig. 2(e).

Although our chemical network does not yet produce model predictions of the N_2H^+ abundance in PDRs and MHDRs, the large range for the N_2H^+/HCN ratio provides more differentiation in modelling the sources. However, the chemistry of N_2H^+ in PDR has been considered elsewhere (Sternberg & Dalgarno 1995) providing (first-order) explanations for the observed behaviour. Given that N_2H^+ is very efficiently destroyed by recombination with electrons (Woodall et al. 2007), the larger average electron abundance (see Fig. 6a) and the higher dissociative recombination rate would remove N_2H^+ from the MHDRs. This figure may also suggest that variation of the UV flux and the resulting electron abundance account for the observed spread of N_2H^+/HCN relative to a systematic change.

The increased electron abundance is primarily caused by the higher temperature in the MHDR and the increased CR ionization rate, both of which reduce the recombination rate of the most abundant ion C^+. The increased CR ionization rate for the MHDR raises the electron abundance by about a factor of 20 (see also McKee 1989), while the mechanical heating component accounts for an increase of a factor about 250 (see Fig. 6a). Similarly, the enhancement of the CR rate for the PDR component would also raise the electron abundance deeper inside the PDR (Boger & Sternberg 2005) and suppress the N_2H^+ abundance. However, the

absence of a clear correlation of the N_2H^+/HCN ratio with R_{Gal} (Fig. 2j) as compared to the distance (Fig. 2e) would confirm that the enhanced CR rate at the GC is not the main contributor to the variation in N_2H^+/HCN. Variations of both the CR rate and the UV flux may account for the variation with R_{Gal} and the increasing spread of the N_2H^+/HCN data points for lower HNC/HCN in Fig. 5(b). Detailed answers on these questions will be found in the ongoing study of the chemistry and radiative transfer of N_2H^+.

6 BOOTSTRAPPING ACROSS SIZE SCALES

The proximity of Galactic emission regions will provide the observer with the most detailed information on their structure and the prevailing physics. Therefore, the molecular characteristics of Galactic star-forming regions may serve as a basis, a benchmark, for studying the partially resolved star formation regions of nearby galaxies and the unresolved emissions of distant starbursts. A comparison of the behaviour of specific molecular properties in varying environments and scales shows both similarities and differences.

6.1 Correlations with IR luminosity

Extragalactic systems exhibit a strong correlation between the FIR luminosity and the luminosity of prominent molecular tracer emissions (Gao & Solomon 2004; Baan et al. 2008). This correlation is analogous to the well-known Kennicutt–Schmidt law (Kennicutt 1998), which relates the star formation density (or L_{FIR}) and the gas surface density (or the line luminosity).

The current Galactic sample alone does not (yet) show clear correlation with L_{FIR}, but on a larger scale our sample fits well on the same relation as found in extragalactic sources (Fig. 7). When including the Galactic sources, the fitted slopes (s2; solid) do not change very much from the extragalactic fit (s1; dashed; Baan et al. 2008). The slopes of HCN and HNC after adding the Galactic data are expectedly similar because of their identical critical densities (see Krumholz & Thompson 2007, for more information). In general, these results are in agreement with the comparable analysis of the HCN–FIR correlation by Wu et al. (2005), which shows less scatter for the Galactic sources. The increased scatter for the Galactic sources in the current L_{mol}–L_{FIR} relations may result partly from the different resolution of the molecular and the 100 μm *IRAS* data (see also Section 5.1).

This linear relation suggests a global scaling law that relates the emission characteristics of nearby star formation regions to those of luminous FIR galaxies. As a first approximation, the properties of extragalactic star formation regions are thus consistent with a scaled up version of Galactic star formation regions. The interpretation of this relation requires many assumptions about the nature of Galactic and extragalactic emission regions.

6.2 Galactic and extragalactic diagnostics

The current Galactic sample is rather heterogeneous and the sources are at different stages of evolution. Nevertheless, they display a well-defined behaviour of their molecular line ratios (e.g. Fig. 3c). Similarly, the extragalactic sample is also comprised of galaxies with different levels of star formation and nuclear activity and at different evolutionary stages, which results in a larger spread of the observed line ratios (e.g. fig. 1 c of Loenen et al. 2008).

Although the environmental conditions for the two classes of sources are found to be very diverse, the characteristics of the integrated emission-line ratios of the two samples are found to be very similar. Our models for the Galactic PDR components suggest similar mean conditions as for conglomerate PDRs of the nuclear regions of ULIRGs (Baan et al. 2008), the only difference being the mean density of the regions. The isolated Galactic PDRs, dominated solely by UV radiation, suggest a slightly higher density range than the nuclear regions of ULIRGs and nearby FIR galaxies. A larger

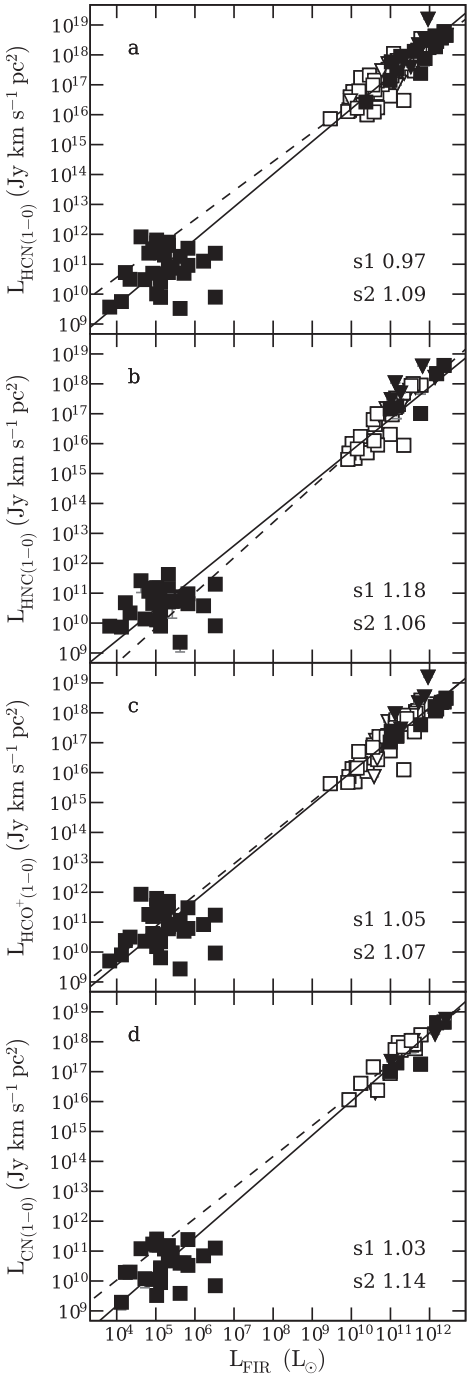

Figure 7. Integrated molecular line luminosities versus L_{FIR} for the sources presented in this work and extragalactic sources (Baan et al. 2008). Symbols for extragalactic sources are open squares for LIRGs, filled squares for ULIRGs and OH megamasers, and triangles for upper limits. Galactic sources are designated by filled squares. The dashed line represents a fit to the extragalactic data (s1) and the solid line (s2) represent a fit to all data with slopes denoted in the lower-right corner of each panel.

range of the density for extragalactic sources may result from the inclusion of a range of intervening lower density components. In addition, the evolutionary sequence of extragalactic starbursts may result in a gradual decrease of average density over evolutionary time (Baan, Loenen & Spaans 2010).

The modelling of the dominant MHDR components in Galactic and extragalactic sources also suggests very similar physical environments, although the actual heating mechanisms are likely to be different. The mechanically heated intervening MHDR gas in extragalactic systems may require a slightly lower temperature and density range (Loenen et al. 2008) than the Galactic MHDR components. In Galactic MHDRs, protostellar outflows are considered to be the most likely heating source considering that they are (relatively) young star-forming systems. Supernova heating (SN) feedback is preferred over outflows in extragalactic sources because it provides the needed energy more easily, and the strongest heating signatures are found in more evolved systems (Baan et al. 2010). A PDR–MHDR mixing sequence will similarly reproduce the observed range of extragalactic line ratios.

In relation to the ionized species, the effects of an enhanced CR ionization rate has been considered for sources close to the GC. While this enhanced CR rate did not (yet) provide much differentiation for the Galactic sources, the shocks resulting from high SN rates and the presence of active galactic nuclei can make the CR a dominant heating and ionization source in extragalactic environments (Papadopoulos 2010).

The first-order similarities found between isolated Galactic and complex and extended extragalactic emission regions provide a basis for comparison and for bootstrapping of star formation activity across a large range of scales. Because similarity does not guarantee identical environments, further interpretation requires more detailed assumptions that describe the structure and the environment of the emission regions. Since significant redundancy remains in the modelling between density, temperature, and the various radiation fields, additional molecular tracers that are sensitive to different environmental characteristics may be used to further differentiate the parameter space of the emission regions.

7 CONCLUSIONS

The sources in this sample were selected as a homogeneous group of star formation regions with UCHIIRs based on their IR properties. In retrospect, the sample is rather diverse as some of the sources do not (yet) have a clearly detected UCHIIR and may be classified as YSOs, Herbig–Haro objects, or simply as IR sources. Nevertheless, the modelling of the line ratios has been done using a single procedure based on the assumption that all sources contain some star-formation-driven PDR-like object accompanied by a possible MHDR component. Because of the fixed beam size, the relative contribution of the two components to the emission lines may also vary with the distance to the source. The modelling procedure seeks to diagnose the diversity of the observed line ratios by using the relative contribution of these two components to the line ratios as an additional parameter. The modelling procedure does not yet incorporate the actual size of the components and their actual line strengths. A next layer of detailed modelling using the spatial information, and the measured FIR and molecular flux densities, will further differentiate among the sample sources.

The modelling of the observed line ratios shows that the relevant parameter space is rather limited for this sample. The line ratios can be explained by modelling them as cold (40–50 K), high-density (10^5–$10^{5.5}$ cm^{-3}) PDRs with a uniform UV flux combined with (possible) MHDRs containing a warm (∼300 K) molecular medium with slightly lower densities ($10^{4.5}$–10^5 cm^{-3}). The MHDR component is not heated by the radiation from the central star (which is attenuated by the central PDR), but rather by mechanical processes, such as protostellar outflows and CR. This aspect already confirms the (early) importance of feedback to heat a larger component of warm molecular gas.

These studies using multimolecular species plus detailed modelling emphasize the strength of this approach in studying the physics and chemistry of the molecular ISM. As the number of molecular species incorporated into these studies is enlarged, the accuracy of the diagnostics will improve, the modelling degeneracy will be reduced, and the amount of information on detailed physics will increase. For example, reproducing the HCO^+ line strengths observed in the sources that are nearby the GC may require the CR ionization rate to be enhanced. The optimal value found of 5×10^{-15} s^{-1} agrees well with previously determined CR ionization rates. Similarly, because the density can be determined using the HCO^+/HCN and HCO^+/HNC line ratios, an accurate estimate of the S-depletion could be made using only a single sulphur-bearing molecule. The optimal range of 200–400 is also in agreement with values found in dense cores of molecular clouds.

Despite the inherent redundancies, the current modelling procedure will be able to describe the global or integrated characteristics of the molecular clouds without looking at the detailed structure inside the region. Details about the internal structure of these regions will follow from modelling of detailed observations of star formation regions at higher resolution. Current modelling also provides physical explanations for the observed differentiation among the sample sources that suggest systematic variations of the global environmental conditions in the sources. Besides the variation in the underlying heating sources and other environmental parameters, also time evolution (i.e. the age) of the star formation region may play a role.

This study also shows that Galactic observations can successfully be used to create a benchmark for extragalactic molecular line studies. Comparing the Galactic and extragalactic line ratios shows that the PDR and MHDR components in both samples have a similar distribution. The MHDR components resulting from non-radiative heating appear less pronounced in the extragalactic systems and require a slightly lower temperature than Galactic sources. This is most likely a result of the increased superposition of different (cold and warm) ISM components in extragalactic systems. The observed similarities in the line ratios between Galactic and extragalactic systems does not automatically invoke a similar nature of the emission regions in these sources. While direct scaling of the regions may be applicable, the exact nature of the environments must be determined by further modelling by including structural information and line strengths. In addition, the inclusion of line ratios of more molecular species with diverse environmental dependences will also help to define the parameters space of the emission regions. However, as long as there are degeneracies in isolating the emission characteristics of distinct components of the ISM, the superposition of different phases of the ISM will continue to complicate the exact interpretation of extragalactic observations.

Single-dish observations of Galactic sources require careful interpretation. The relatively large beam sizes make observations sensitive to geometrical effects and a superposition of completely different components of the ISM. Identification of these different ISM components in order to increase their detailed structure requires the enhanced spatial resolution of interferometers. Furthermore,

increased spectral coverage and access to molecular and atomic transitions will provide more complexity and accuracy of the theoretical modelling of Galactic sources.

ACKNOWLEDGEMENTS

The authors thank the referee for the positive and constructive comments regarding this paper. This work has benefited from research funding from the European Community's Sixth Framework Programme under RadioNet R113CT 2003 5058187. This research has made use of the SIMBAD data base, operated at CDS, Strasbourg, France. WAB acknowledges the Chinese Academy of Science for the Visiting Foreign Scholar appointment at the Shanghai Astronomical Observatory, where the final part of this work was done.

REFERENCES

Aalto S., Polatidis A. G., Hüttemeister S., Curran S. J., 2002, A&A, 381, 783
Aalto S., Spaans M., Wiedner M. C., Hüttemeister S., 2007, A&A, 464, 193
Baan W. A., Henkel C., Loenen A. F., Baudry A., Wiklind T., 2008, A&A, 477, 747
Baan W. A., Loenen A. F., Spaans M., 2010, A&A, 516, A40
Bachiller R., Perez Gutierrez M., 1997, ApJ, 487, L93
Bayet E., Williams D. A., Hartquist T. W., Viti S., 2011, MNRAS, 414, 1583
Beichman C. A., Neugebauer G., Habing H. J., Clegg P. E., Chester T. J. eds 1988, Infrared Astronomical Satellite (IRAS) Catalogs and Atlases. Volume 1: Explanatory Supplement. NASA, Washington, DC
Beuther H., Schilke P., Sridharan T. K., Menten K. M., Walmsley C. M., Wyrowski F., 2002, A&A, 383, 892
Boger G. I., Sternberg A., 2005, ApJ, 632, 302
Bourke T. L., Hyland A. R., Robinson G., 2005, ApJ, 625, 883
Bronfman L., Nyman L.-A., May J., 1996, A&AS, 115, 81
Broos P. S., Feigelson E. D., Townsley L. K., Getman K. V., Wang J., Garmire G. P., Jiang Z., Tsuboi Y., 2007, ApJS, 169, 353
Codella C., Bachiller R., Reipurth B., 1999, A&A, 343, 585
Devereux N. A., Young J. S., 1990, ApJ, 359, 42
Draine B. T., 1978, ApJS, 36, 595
Faure A., Lique F., 2012, MNRAS, 425, 740
Ferland G. J., Fabian A. C., Hatch N. A., Johnstone R. M., Porter R. L., van Hoof P. A. M., Williams R. J. R., 2009, MNRAS, 392, 1475
Field G. B., Goldsmith D. W., Habing H. J., 1969, ApJ, 155, L149
Fuente A., Martin-Pintado J., Gaume R., 1995, ApJ, 442, L33
Fuente A., García-Burillo S., Gerin M., Teyssier D., Usero A., Rizzo J. R., de Vicente P., 2005, ApJ, 619, L155
Gao Y., Solomon P. M., 2004, ApJS, 152, 63
Goicoechea J. R., Pety J., Gerin M., Teyssier D., Roueff E., Hily-Blant P., Baek S., 2006, A&A, 456, 565
Gondhalekar P. M., 1985, MNRAS, 217, 585
Graciá-Carpio J., García-Burillo S., Planesas P., Colina L., 2006, ApJ, 640, L135
Habing H. J., 1968, Bull. Astron. Inst. Neth., 19, 421
Hollenbach D. J., Tielens A. G. G. M., 1999, Rev. Mod. Phys., 71, 173
Jones P. A. et al., 2008, MNRAS, 386, 117
Kazandjian M. V., Meijerink R., Pelupessy I., Israel F. P., Spaans M., 2012, A&A, 542, A65
Kennicutt R. C., Jr, 1998, ApJ, 498, 541
Krumholz M. R., Thompson T. A., 2007, ApJ, 669, 289
Lo N. et al., 2009, MNRAS, 395, 1021
Loenen A. F., Baan W. A., Spaans M., 2006, A&A, 458, 89
Loenen A. F., Spaans M., Baan W. A., Meijerink R., 2008, A&A, 488, L5
López-Sepulcre A., Cesaroni R., Walmsley C. M., 2010, A&A, 517, A66
López-Sepulcre A. et al., 2011, A&A, 526, L2
McKee C. F., 1989, ApJ, 345, 782
Meijerink R., Spaans M., 2005, A&A, 436, 397
Meijerink R., Spaans M., Israel F. P., 2006, ApJ, 650, L103
Meijerink R., Spaans M., Israel F. P., 2007, A&A, 461, 793
Norman C. A., Ferrara A., 1996, ApJ, 467, 280
Oka T., Hasegawa T., Sato F., Tsuboi M., Miyazaki A., 1998, ApJS, 118, 455
Oka T., Geballe T. R., Goto M., Usuda T., McCall B. J., 2005, ApJ, 632, 882
Ott J., Weiss A., Henkel C., Walter F., 2005, ApJ, 629, 767
Padovani M., Galli D., 2013, in Torres D. F., Reimer O., eds, Astrophysics and Space Science Proc. Vol. 34, Cosmic Rays in Star-Forming Environments. Springer-Verlag, Berlin, p. 61
Papadopoulos P. P., 2010, ApJ, 720, 226
Qiu K., Zhang Q., Beuther H., Yang J., 2007, ApJ, 654, 361
Ramesh B., Sridharan T. K., 1997, MNRAS, 284, 1001
Reid M. A., Matthews B. C., 2008, ApJ, 675, 1343
Ruffle D. P., Hartquist T. W., Caselli P., Williams D. A., 1999, MNRAS, 306, 691
Schilke P., Walmsley C. M., Pineau Des Forets G., Roueff E., Flower D. R., Guilloteau S., 1992, A&A, 256, 595
Simon R., Jackson J. M., Clemens D. P., Bania T. M., Heyer M. H., 2001, ApJ, 551, 747
Solomon P. M., Rivolo A. R., Barrett J., Yahil A., 1987, ApJ, 319, 730
Solomon P. M., Downes D., Radford S. J. E., 1992, ApJ, 387, L55
Spaans M., 1996, A&A, 307, 271
Sridharan T. K., Beuther H., Schilke P., Menten K. M., Wyrowski F., 2002, ApJ, 566, 931
Sternberg A., Dalgarno A., 1995, ApJS, 99, 565
Talbi D., Ellinger Y., Herbst E., 1996, A&A, 314, 688
Tieftrunk A., Pineau des Forets G., Schilke P., Walmsley C. M., 1994, A&A, 289, 579
van der Wiel M. H. D., van der Tak F. F. S., Ossenkopf V., Spaans M., Roberts H., Fuller G. A., Plume R., 2009, A&A, 498, 161
Wada K., Norman C. A., 2007, ApJ, 660, 276
Weiß A., Downes D., Neri R., Walter F., Henkel C., Wilner D. J., Wagg J., Wiklind T., 2007, A&A, 467, 955
Wolfire M. G., Hollenbach D., McKee C. F., Tielens A. G. G. M., Bakes E. L. O., 1995, ApJ, 443, 152
Woodall J., Agúndez M., Markwick-Kemper A. J., Millar T. J., 2007, A&A, 466, 1197
Wu Y., Wei Y., Zhao M., Shi Y., Yu W., Qin S., Huang M., 2004, A&A, 426, 503
Wu J., Evans N. J., II, Gao Y., Solomon P. M., Shirley Y. L., Vanden Bout P. A., 2005, ApJ, 635, L173

APPENDIX A: ^{13}CO AND C^{18}O RELATIONS

No clear trends were found when comparing the ^{13}CO and C^{18}O data to the high-density tracers, unlike what has been found for galaxies (Baan et al. 2008). Only the two HNC/CO line ratios display a decrease as a function of distance from the source (figure not shown here), which is likely caused by the decrease in the HNC line strength (see Section 5.2). Fig. A1 shows that the ^{13}CO/C^{18}O ratio remains relatively constant with distance throughout the sample. The ^{13}CO line will be slightly optically thick in most sources, which results in ratios just below the expected (solar) ratio as denoted by the dotted line. At larger distances (beyond 4.5 kpc), the spread in the data points becomes larger and some ratios are above the solar value but compatible within the errors. Because of the large physical size of the beam at those distances, the observing beam will also include more extended CO components with a range of optical depths for the ^{13}CO line. This would indicate that both CO lines also trace a large-scale component of the ISM, which does not necessarily relate to the star formation activity.

Table A1. List of sources and observed line strengths. The errors are given within parentheses. Ellipses indicate non-detections.

Source IRAS	R_{Gal} (kpc)	Dist. (kpc)	Velo. (km s^{-1})	L_{FIR} (log L$_\odot$)	^{13}CO (1–0) (Jy km s^{-1})		C^{18}O (1–0) (Jy km s^{-1})		HCN (1–0) (Jy km s^{-1})		HNC (1–0) (Jy km s^{-1})		HCO$^+$ (1–0) (Jy km s^{-1})		CS (2–1) (Jy km s^{-1})		CN (1–0) (Jy km s^{-1})		N$_2$H$^+$ (1–0) (Jy km s^{-1})	
00206+6555	13.5	7.0	−68.4	4.3	160.7	(2.9)	16.1	(6.2)	54.2	(3.5)	37.8	(7.9)	54.7	(2.6)	45.7	(5.7)	34.4	(12.7)	–	–
00338+6312	9.4	1.6	−17.7	5.0	357.1	(10.9)	49.6	(2.7)	338.0	(5.5)	423.1	(15.9)	504.7	(9.4)	309.1	(11.9)	108.6	(14.4)	315.2	(4.6)
00340+6619	10.9	3.7	−39.9	3.8	126.3	(4.9)	17.6	(4.6)	22.8	(4.0)	48.9	(11.5)	31.1	(3.2)	29.5	(6.3)	–	–	–	–
00342+6347	10.1	2.6	−28.4	4.1	176.3	(9.6)	28.4	(5.6)	70.8	(8.8)	92.1	(12.1)	100.5	(16.9)	89.3	(20.9)	24.4	(10.7)	101.6	(6.2)
18151−1208	5.7	13.1	+32.8	5.0	358.3	(31.9)	32.4	(15.5)	318.2	(28.9)	75.9	(48.2)	307.0	(16.4)	539.8[a]	(217.5)[a]	124.8	(78.8)	70.8	(15.2)
18228−1312	5.7	13.1	+33.3	5.3	431.4	(23.6)	146.9	(32.3)	210.0	(26.0)	208.5	(57.9)	244.0	(35.2)	193.4[a]	(78.1)[a]	–	–	147.3	(18.6)
18264−1152	5.3	12.4	+43.6	4.6	345.6	(22.0)	26.7	(10.2)	453.1	(94.2)	143.9	(85.9)	471.2	(30.9)	98.7[a]	(39.1)[a]	66.2	(5.1)	170.8	(17.9)
18311−0809	3.6	8.9	+113.9	4.8	385.4	(32.4)	66.9	(19.1)	251.0	(295.6)	124.0	(21.2)	193.4	(26.5)	–[a]	–[a]	–	–	142.0	(20.6)
18314−0720	3.9	9.3	+103.2	5.3	660.2	(41.8)	90.1	(19.6)	535.6	(34.4)	132.4	(25.2)	307.2	(18.9)	–[a]	–[a]	150.0	(72.5)	90.4	(18.9)
18317−0513	5.9	12.1	+42.2	5.0	246.6	(126.8)	41.3	(18.3)	299.0	(22.9)	56.8	(10.7)	208.9	(8.9)	–[a]	–[a]	91.4	(20.0)	75.5	(23.9)
18317−0757	4.4	10.5	+79.3	5.1	363.9	(40.7)	120.9	(40.3)	185.7	(28.9)	26.3	(12.3)	140.1	(23.5)	–[a]	–[a]	–	–	78.5	(20.1)
18341−0727	3.7	8.8	+113.0	4.9	463.0	(24.6)	97.0	(13.7)	357.9	(68.4)	160.8	(37.9)	169.1	(19.1)	–[a]	–[a]	188.2	(40.2)	103.6	(19.8)
19410+2336	7.6	6.1	+22.4	5.2	372.9	(13.2)	72.9	(16.2)	460.5	(17.5)	167.0	(27.4)	528.3	(52.8)	217.2[a]	(22.3)[a]	267.6	(19.8)	250.0	(11.4)
19442+2427	7.6	5.8	+21.7	5.8	684.4	(31.2)	68.8	(14.5)	860.7	(38.1)	239.9	(90.2)	761.3	(75.3)	296.4	(27.0)	612.0	(56.7)	167.1	(34.2)
19446+2505	7.6	5.5	+21.9	6.2	415.2	(8.7)	56.5	(24.9)	354.8	(19.8)	106.1	(183.0)	233.3	(58.5)	67.8	(14.9)	194.8	(24.0)	–	–
20188+3928	8.4	3.2	+2.1	5.3	503.1	(51.5)	67.4	(9.0)	436.0	(18.7)	421.8	(51.2)	586.4	(31.7)	308.5	(37.7)	388.4	(22.8)	386.2	(11.6)
20231+3440	8.3	3.7	+5.4	4.2	244.2	(8.3)	48.7	(8.8)	326.5	(26.2)	297.1	(23.4)	150.6	(20.8)	186.2	(15.1)	120.0	(20.8)	249.7	(18.7)
20286+4105	8.7	3.7	−3.9	5.3	406.7	(12.4)	55.5	(68.9)	508.9	(15.6)	322.8	(15.6)	371.5	(99.6)	280.4	(77.1)	525.2	(22.1)	143.4	(12.2)
20293+3952	8.3	2.9	+6.3	5.1	570.3	(17.7)	78.2	(8.4)	248.6	(28.1)	301.0	(135.4)	222.7	(30.2)	147.9	(70.1)	278.1	(22.3)	187.0	(10.4)
21078+5211	8.8	1.8	−6.4	5.6	207.1	(25.7)	30.5	(7.2)	86.9	(7.7)	59.9	(31.6)	71.3	(5.0)	65.5	(6.7)	100.8	(15.3)	6.3	(12.8)
21334+5039	10.7	5.9	−44.1	5.1	342.8	(24.9)	34.8	(5.3)	116.6	(12.4)	51.8	(6.0)	93.0	(15.3)	83.2	(15.5)	35.5	(10.2)	–	–
21413+5442	12.2	7.6	−63.9	5.6	183.3	(7.9)	16.4	(5.8)	268.8	(27.5)	111.2	(7.8)	168.0	(6.0)	139.6	(8.2)	57.7	(68.7)	25.3	(9.5)
21418+5403	11.9	7.2	−59.9	4.7	181.3	(11.0)	15.9	(4.8)	50.0	(9.3)	22.5	(5.7)	37.7	(5.3)	42.4	(14.4)	19.6	(9.8)	–	–
22134+5834	9.3	2.3	−18.3	5.1	401.0	(16.6)	47.5	(4.1)	124.8	(16.0)	126.7	(17.9)	102.9	(10.2)	84.7	(23.8)	142.0	(24.8)	57.7	(5.8)
22506+5944	11.4	5.3	−51.2	4.9	315.3	(6.0)	25.6	(4.2)	150.5	(20.8)	136.9	(13.2)	126.2	(8.0)	123.6	(13.9)	34.0	(8.9)	38.1	(4.9)
22539+5758	11.6	5.7	−54.1	5.1	356.4	(11.3)	46.5	(4.3)	90.4	(13.3)	62.6	(15.2)	62.6	(9.3)	81.1	(8.6)	65.3	(12.7)	20.2	(4.1)
22543+6145	9.0	1.2	−11.1	6.5	827.2	(38.1)	164.0	(6.1)	466.7	(57.7)	476.7	(15.2)	545.2	(16.3)	328.2	(37.5)	409.4	(24.8)	253.1	(8.3)
22566+5830	11.3	5.2	−50.3	5.7	400.0	(76.2)	47.2	(13.5)	155.9	(11.4)	170.2	(21.1)	155.6	(24.4)	115.5	(17.3)	128.7	(17.6)	74.4	(5.7)
23033+5951	11.6	5.5	−53.1	5.4	177.1	(58.3)	55.5	(6.2)	205.8	(22.3)	148.3	(107.3)	235.0	(44.7)	125.5	(12.0)	245.4	(33.8)	122.7	(7.8)
23116+6111	11.9	5.8	−57.2	6.5	821.6	(51.9)	90.3	(8.4)	586.1	(29.0)	503.3	(19.6)	430.5	(24.9)	523.8	(33.0)	317.8	(22.2)	142.2	(6.7)
23138+5945	10.9	4.4	−44.1	5.8	472.7	(7.2)	27.8	(31.4)	401.1	(18.5)	194.3	(7.6)	269.0	(5.1)	187.1	(7.5)	145.6	(15.8)	81.9	(6.5)
19102+0906[b]	7.8	11.5	+12.2	–[b]	1431.8	(44.3)	177.6	(27.9)	1197.2	(119.9)	442.6	(58.0)	1217.2	(29.7)	860.2	(58.0)	435.9	(36.2)	106.3	(29.6)

[a]Inclement weather conditions.
[b]Not an *IRAS* source, name indicates position.

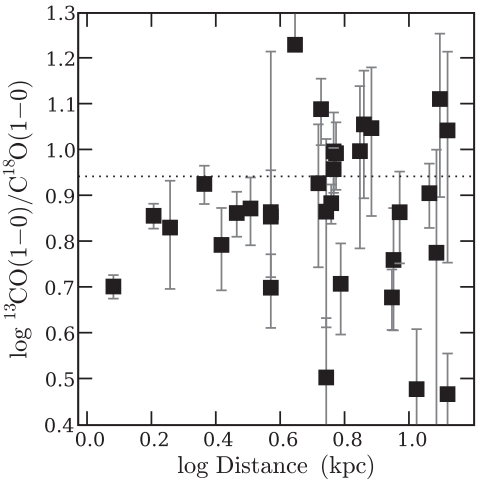

Figure A1. Integrated line ratio of the two observed CO isotopes versus distance. The dotted line shows the solar ^{13}CO/C^{18}O isotope ratio.

SUPPORTING INFORMATION

Additional Supporting Information may be found in the online version of this paper:

APPENDIX B: SPECTRA (http://www.mnras.oxfordjournals.org/lookup/suppl/doi:10.1093/mnras/stu1897/-/DC1).

Please note: Oxford University Press is not responsible for the content or functionality of any supporting materials supplied by the authors. Any queries (other than missing material) should be directed to the corresponding author for the paper.

This paper has been typeset from a TEX/LATEX file prepared by the author.